Satellite Microwave Remote Sensing of Boreal and Arctic Soil Temperatures From AMSR-E

Lucas A. Jones, *Student Member, IEEE*, John S. Kimball, Kyle C. McDonald, *Senior Member, IEEE*, Steven Tsz K. Chan, *Senior Member, IEEE*, Eni G. Njoku, *Fellow, IEEE*, and Walter C. Oechel

***Abstract*—Methods are developed and evaluated to retrieve surface soil temperature information for the Advanced Microwave Scanning Radiometer on Earth Observing System for seven boreal forest and Arctic tundra biophysical monitoring sites across Alaska and Northern Canada. A multiple-band iterative radiative transfer process-based method producing dynamic vegetation and snow cover correction quantities and an empirical multiple regression method using several frequencies are employed. The seasonal pattern of microwave emission and relative accuracy of the soil temperature retrievals are influenced strongly by landscape properties, including the presence of open water, vegetation type and seasonal phenology, snow cover, and freeze–thaw transitions. The retrieval of soil temperature is similar for the two methods with an overall root-mean-square error of 3.1–3.9 K during summer thawed conditions, with a larger error occurring in winter during periods of dynamic snow cover and freeze–thaw state. These results indicate that at high latitudes, the influence of the atmosphere may be less important than that of surface conditions in determining the relative accuracy of the estimated soil temperature. Impacts of surface conditions on surface emissivity, observed brightness temperature, and estimated soil temperature are discussed.**

***Index Terms*—Advanced Microwave Scanning Radiometer for the Earth Observing System (AMSR-E), Arctic tundra, boreal forest, microwave radiometry, satellite remote sensing, soil temperature.**

I. Introduction

OBSERVATIONAL evidence indicates that mean annual surface temperatures in Arctic and boreal regions have warmed 2 °C to 4 °C in the last several decades [1]–[3]. Global model projections indicate that warming under future climate change will be most pronounced in high-latitude regions [4], [5]. Warming is expected to alter the surface energy balance and hydrologic systems, with resulting feedback to climate [6]. High-latitude regions have a sparse network of meteorological stations, which strongly limits capabilities for regional monitoring of climate change. Accurate surface meteorological information also provides critical inputs for regional-scale terrestrial and hydrological models. The largest error in the Moderate Resolution Imaging Spectroradiometer (MODIS) MOD17 terrestrial productivity products was introduced by uncertainties in daily surface meteorology inputs [7]. The latest generation of Earth Observing System (EOS) satellite remote-sensing-based observations provides an unprecedented array of global daily monitoring capabilities at moderate spatial resolution, including multiband optical–infrared (IR) and passive microwave-based measurements from MODIS and Advanced Microwave Scanning Radiometer for the Earth Observing System (AMSR-E), respectively. These measurements are sensitive to thermal and moisture characteristics of the land surface and provide a potential alternative to spatially gridded meteorological data from sparse surface station networks and model reanalyses for driving terrestrial ecosystem models.

Soil temperature is a crucial variable for characterizing the surface energy balance, permafrost heating, and soil organic matter decomposition, which is also a significant source of high-latitude terrestrial carbon emissions (both CO_2 and CH_4) to the atmosphere [6], [8], [9]. Satellite IR remote sensing observations from the National Oceanic and Atmospheric Administration Advanced Very High Resolution Radiometer and National Aeronautics and Space Administration (NASA) MODIS have been widely used for the retrieval of land surface temperature information [10]–[12]. Satellite passive microwave sensors such as the Special Sensor Microwave/Imager (SSM/I) and Scanning Multichannel Microwave Radiometer have also been used to retrieve land surface temperature [13]–[17]. Despite having a coarse spatial resolution ($>$ 5 km) relative to optical–IR remote sensing, longer wavelength microwave sensors are less impacted by cloud cover, smoke, and atmospheric aerosol effects and can retrieve surface information day or night regardless of solar illumination conditions. This represents a significant advantage over optical–IR remote sensing for regional monitoring at high latitudes. Microwave emission at low frequencies, e.g., C-band ($\sim$6.9 GHz) and L-band ($\sim$1.4 GHz), responds to temperature conditions under vegetation and below the soil surface, although direct sensitivity to these deeper microwave emitting layers decreases under increasing vegetation water content and soil moisture levels [14]. The emitting soil layer is shallower, and the vegetation opacity is greater

Manuscript received June 27, 2006; revised April 13, 2007. This work was carried out at the University of Montana and at the Jet Propulsion Laboratory, California Institute of Technology, under contract to the National Aeronautics and Space Administration.

L. A. Jones is with the Numerical Terradynamic Simulation Group, College of Forestry and Conservation, University of Montana, Missoula, MT 59812 USA, and also with the Flathead Lake Biological Station, University of Montana, Polson, MT 59860 USA (e-mail: lucas@ntsg.umt.edu).

J. S. Kimball is with the School of Forestry/Numerical Terradynamic Simulation Group, University of Montana, Polson, MT 59860-9659 USA (e-mail: johnk@ntsg.umt.edu).

K. C. McDonald, S. T. K. Chan, and E. G. Njoku are with the Jet Propulsion Laboratory, California Institute of Technology, Pasadena, CA 91109-8001 USA (e-mail: kyle.mcdonald@jpl.nasa.gov; Steven.K.Chan@jpl.nasa.gov; Eni.G.Njoku@jpl.nasa.gov).

W. C. Oechel is with Global Change Research Group, San Diego State University, San Diego, CA 92182 USA (e-mail: oechel@sunstroke.sdsu.edu).

Color versions of one or more of the figures in this paper are available online at http://ieeexplore.ieee.org.

Digital Object Identifier 10.1109/TGRS.2007.898436

0196-2892/$25.00 © 2007 IEEE

TABLE I
BIOPHYSICAL NETWORK SITES USED FOR THIS INVESTIGATION. NSA NOBS REFERS TO THE NORTHERN STUDY AREA OLD BLACK SPRUCE, AND SSA OAS REFERS TO THE SOUTHERN STUDY AREA OLD ASPEN TOWER SITES LOCATED WITHIN THE BOREAL ECOSYSTEM–ATMOSPHERE STUDY (BOREAS) REGION OF CENTRAL CANADA. THESE SITES ARE CURRENTLY ASSOCIATED WITH THE BOREAL ECOSYSTEM MONITORING AND RESEARCH SITES PROJECT

Site	Abbrev.	Location	Lat. Long.	Vegetation	Topog.
Barrow	BRW	Arctic Coast Alaska	71.32 N 156.62 W	Wet-sedge Tundra	flat
Atqasuk	ATQ	N. Slope Alaska	70.47 N 157.40 W	Wet-sedge Tundra	flat
Ivotuk	IVO	N. Slope Alaska	68.47 N 155.73 W	Tussock Tundra	foothills
Happy Valley/Sagwon	HPV	N. Slope Alaska	69.13 N 148.83 W	Tussock Tundra	foothills
NSA NOBS	NOBS	N. Manitoba	55.88 N 98.48 W	Boreal spruce forest	flat
SSA OAS	OAS	N. Sask.	53.63 N 106.20 W	Boreal aspen forest	flat
Lethbridge	LTH	S. Alberta	49.70 N 112.93 W	Grassland	flat

for higher frequency microwave observations. The emitting depth is typically between 0.5 and 2.8 cm at C-band for soil volumetric moisture contents of 10% and 50%, respectively, assuming a soil bulk density of 1.50 g cm^{-3}, which is typical of tundra soils [14]. Frequencies of 10.7 GHz and lower may be susceptible to radio frequency interference (RFI) near densely populated areas depending on the bandwidth, center frequency, and polarization of the anthropogenic radiation and characteristics of the observing sensor [18], [19]; however, this may not be a significant problem in sparsely populated high-latitude regions. Passive microwave observations are also sensitive to surface wetness [20]–[22], vegetation biomass [23]–[25], and freeze–thaw state [26], [27].

Difficulty in retrieving surface temperature from the SSM/I under snow-covered and open water surface conditions over the central plains of the U.S. was reported by McFarland *et al.* [13]. Many studies have since devised methods for dealing with diverse land cover types. A spectral difference method was applied to derive screen-height (2 m) air temperatures from the SSM/I over open water and snow cover in the continental U.S. [16]. A polarization ratio method was applied to retrieve soil temperatures from a tower-based radiometer over a variety of land cover conditions in Switzerland [28] and from SSM/I 19-GHz brightness temperatures under both frozen and snow-covered winter surfaces [29]. This method was also employed for surface temperature retrieval in the boreal forest of Finland and was reported to have larger error over dense vegetation than an empirical multiple-regression method [15]. A similar polarization ratio method was applied to retrieve surface temperature and surface water fraction over wet Arctic and boreal regions of northern Canada under snow-free conditions [17]. Iterative inversion of radiative transfer equations has also been used [15], as well as learning algorithms including neural networks, which have been suggested for dealing with surface heterogeneity [30]; both methods require either a great deal of *a priori* information on land cover parameters or large training data sets.

The objectives of the current investigation are: 1) to evaluate the spatial and seasonal dynamics of multifrequency AMSR-E brightness temperature data relative to surface biophysical station observations of daily soil profile and air temperatures and 2) to compare two alternate approaches to retrieve soil temperature information from AMSR-E under temporally dynamic surface physical conditions and for boreal forest and Arctic tundra biomes represented by seven monitoring sites. We develop and apply two algorithms to retrieve surface (< 5 cm) soil temperature over boreal forest, tundra, and grassland biomes of Alaska and Canada using the AMSR-E onboard the NASA EOS Aqua satellite for future use in biophysical modeling at high latitudes. Our approach employs *in situ* soil temperature data for fitting parameters and assessing algorithm performance; these data were collected at three Ameriflux, three FLUXNET Canada eddy-covariance flux towers [31], and one Kuparuk river basin site administered by the University of Alaska Fairbanks Water and Environmental Research Center [32], which is located in five distinct vegetation and land cover regimes representing major boreal forest and Arctic tundra biomes. The satellite data are from footprint extractions of spatially resampled AMSR-E L2A orbital-swath data centered at each tower location.

II. STUDY SITES AND DATA

A. Biophysical Network Sites

The seven study sites are representative of five distinct vegetation types (Table I; Fig. 1). The vegetation types are coastal lowland wet sedge tundra, upland tussock tundra, boreal evergreen forest, boreal deciduous forest, and boreal grassland. Tundra landscapes are generally a mosaic of tussock and sedge tundra vegetation types; however, for convenience, the tundra sites were grouped according to the dominant vegetation type. Wet sedge tundra dominates in moist poorly drained lowland and coastal areas, whereas tussock tundra dominates the drier upland/foothill sites. Coastal wet sedge tundra is represented by the Barrow (BRW) and Atqasuk (ATQ) sites and is characterized by low topography and a shallow water table with numerous thaw lakes. The vegetation is predominantly composed of low-growing sedges and mosses, interspersed with areas of shallow standing water. Soils are highly organic and consist of a shallow active layer that thaws each growing season and is underlain by continuous permafrost [33]. Wet sedge tundra lacks the hummocky microtopography of tussock tundra but may contain polygonal features formed by frost-wedge action, which consist of flat surfaces surrounded by shallow troughs. Tussock tundra at Ivotuk (IVO) and Happy Valley (HPV) is characterized by *Eriophorum vaginatum*, which is also known as "cotton grass," and low shrubs [34]. These two sites are located within ~40 km of the Brooks Range, and the soil active layer tends to be thicker than that of coastal sites [35].

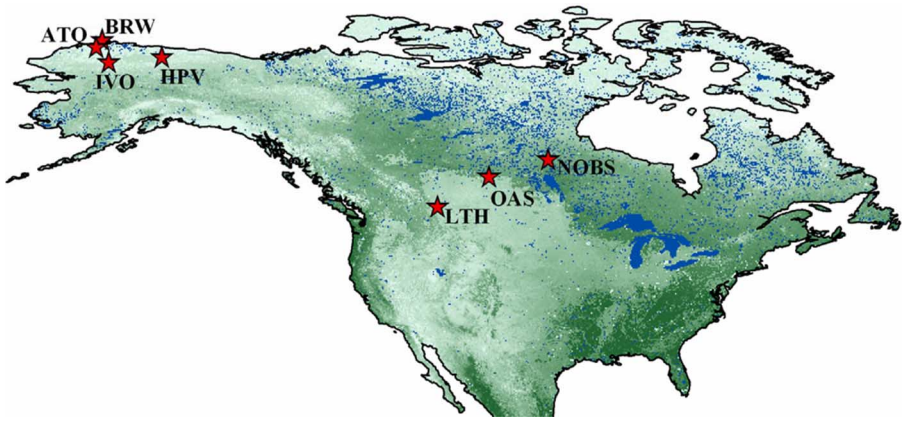

Fig. 1. Biophysical network sites.

TABLE II
AMSR-E INSTRUMENT SPECIFICATIONS

Center Frequency (GHz)	6.9	10.7	18.7	23.8	36.5	89.0
Bandwidth (MHz)	350	100	200	400	1000	3000
3-dB Footprint (km)	75 x 43	51x 29	27 x 16	32 x 18	14 x 8	6 x 4
Resolution (km)	60	60	25	25	15	5

The boreal sites are located in Central Canada. Boreal evergreen coniferous forest is represented by the Northern Old Black Spruce (NOBS) site and is dominated by mature black spruce (*Picea marianna*) forest with a canopy height of 10–13 m and low topographic relief [36]. The Old Aspen (OAS) site is composed of deciduous broad-leaf boreal forest dominated by aspen (*Populus tremuloides*) with a mean canopy height of 21 m and low topographic relief [37]. The Lethbridge (LTH) boreal grassland site is the southernmost study site and is composed of semiarid short-grass prairie on relatively flat terrain [38].

B. In Situ Observations

Soil temperatures were obtained from tower and hydrologic monitoring site investigators. Soil temperature data were recorded at a variety of measurement depths at each location. The 0- to 5-cm depth was selected as the primary focus of this investigation because it was readily available across all study sites. Although lower range of this depth is greater than the expected microwave emitting depth of 2.5 cm at C-band or less for higher frequencies and greater soil moisture levels [14], we observed that daily temperature differences between near-surface soil depths and daily minimum air temperatures (above and below canopy for forested sites) are highly correlated with brightness temperatures under all conditions ($r > 0.70$; $P < 0.001$). For simplicity, we assumed that the near-surface soil profile (e.g., < 5 cm) is generally isothermal. Vertical and horizontal heterogeneity in soil temperature within and across the field-of-view also potentially adds variability to the brightness temperature observations. For this reason, we compare the surface temperature retrievals to three independent measures of the surface temperature. Comparison with T_{soil} and T_{min} bracket the possible extremes in surface temperature, whereas MODIS Land Surface Skin Temperature (LST) observations are used to assess subgrid-scale spatial heterogeneity in surface temperature conditions within the AMSR-E footprint. Soil and air temperature measurements from the study sites were reported at 30-min intervals and aggregated to daily minimums for comparison with daily satellite morning (A.M.) overpass observations. Daily minimums of soil temperature (5 cm) were not significantly different ($p > 0.05$) from the temperature at overpass time and the temperature at time of the minimum temperature gradient between the 2- and 5-cm depths at all sites. This assumption holds well for Arctic and boreal soils, which have a large amount of thermal inertia relative to drier midlatitude soils, which are subjected to more intense diurnal heating. The *in situ* data were obtained from June 2002 to December 2004 to coincide with AMSR-E observations, which began with the launch of the Aqua satellite in May 2002.

C. Satellite Data

The AMSR-E flies on the Aqua satellite platform and measures brightness temperatures at frequencies of 6.9, 10.7, 18.7, 23.8, 36.5, and 89 GHz for vertical and horizontal polarizations (Table II). Aqua is polar orbiting with 1 A.M./P.M. equatorial crossing times, providing multiple daily acquisitions in polar regions [39]. For high-latitude regions, the overlapping orbital swaths allow two to four T_b observations per footprint overpass with a typical standard deviation of $\sim$1 K ($\max = 5$ K) at 6.9 GHz and < 1 K ($\max = 3.5$ K) at 89 GHz. T_b measurements were extracted at each test site from the AMSR-E level 2A orbital swath data spatially resampled to the $\sim$60-km 6.9-GHz resolution [40]. The T_b observations were only extracted from sensor footprints whose centroid falls within 5 km of each tower location. Therefore, the observations can be considered to be representative of a $\sim$60-km pixel centered at the tower location. The minimum T_b of the descending (A.M.) overpass was selected on a daily basis for each site location under the assumption that the diurnal temperature minimum is more representative of surface soil layer temperatures. The descending overpass occurs from 3 to 6 A.M. local time in the study region and was chosen because the near-surface soil

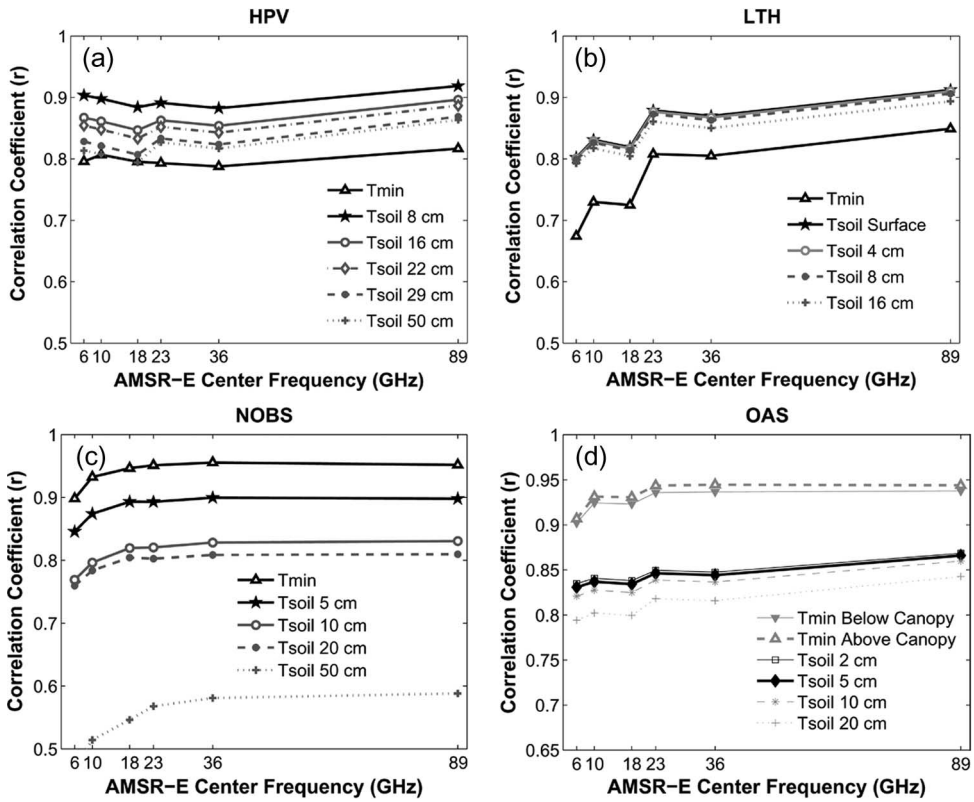

Fig. 2. Linear correlation between AMSR-E uncorrected T_{bv} values for various frequencies and *in situ* minimum daily air temperature $T_{\min}$ and soil temperature T_{soil} measurements for selected study sites. Note that the soil and air temperature measurement levels are different for each plot, as measurement depth differed between each site.

and air temperatures were expected to be closer to thermal equilibrium.

The brightness temperatures were inspected for RFI using the difference between the 6.9- and 10.7-GHz channels and the difference between the 10.7- and 18.7-GHz channels developed by Njoku *et al.* [18]. For LTH, where RFI was expected to be most severe, a mean thawed condition RFI index for the 6.9-GHz (10.7-GHz) band V-polarization of 0.51 K (-0.25 K) and a standard deviation of 0.99 K (1.11 K) were calculated. These values are well below the 3 K (6.9 GHz) and -0.25 K (10.7 GHz) index thresholds suggested for identifying moderate to strong RFI [18]. The H-polarization mean 6.9-GHz and 10.7-GHz RFI indexes were similarly small (0.14 K for 6.9 GHz and 0.14 K at 10.7 GHz) at LTH. The RFI index for the 6.9-GHz band did range as high as 9.0 K for frozen conditions, but these are assumed to be the effects of snow cover and not of RFI. These results indicate that moderate RFI was not detected in either the 6.9-GHz or the 10.7-GHz channel at H- or V-polarization at the study sites, and filtering of the brightness temperatures for RFI was not necessary.

Land cover heterogeneity within each AMSR-E tower footprint was assessed by extracting 60×60 km windows centered on each tower site from the MODIS 1-km resolution global land cover classification [41]. The MODIS land cover extraction subsets were obtained from the Oak Ridge National Laboratory Distributed Active Archive Center [42]. Relative proportions of the International Geosphere–Biosphere Program-based land cover classes were calculated from the MODIS land cover classification results within each window.

D. Land Cover Effects on the Correlation of T_b to In Situ Temperatures

The MODIS land cover windows indicated that BRW and ATQ had the greatest amount of open water with 87% and 12% respective coverage. The other sites had $< 6\%$ open water. Tundra vegetation at BRW, ATQ, IVO, and HPV was classified as open shrubland, which varied in areal extent from 9% at BRW to 97% at HPV, and as grassland, which varied in extent from 25% at ATQ to $< 3\%$ at the other tundra sites. Grassland coverage was dominant at LTH (56%), followed by cropland (41%). Evergreen needleleaved forest was dominant at NOBS (77%) but was also present at OAS (15%). The OAS window also had significant proportions of mixed forest (36%) and croplands (39%). Urban areas were present at LTH and NOBS but represented $< 1\%$ of the total window area.

Land cover is expected to influence the correlation between T_b and physical surface temperature by shifting the soil and vegetation layers in which the physical temperature contributes most strongly to the bulk signal and by modifying the overall emissivity of the scene. Therefore, simple linear correlation coefficients were computed between daily time series AMSR-E V-polarized T_b and available *in situ* soil and near-surface air temperature measurements under thawed conditions to gain an understanding of the relation between sensor T_b from individual bands and the surface temperature profile for each study site (Fig. 2). Previous studies have shown that V-polarized T_b is generally more sensitive to surface temperature than H-polarized T_b [13], [14], presumably because

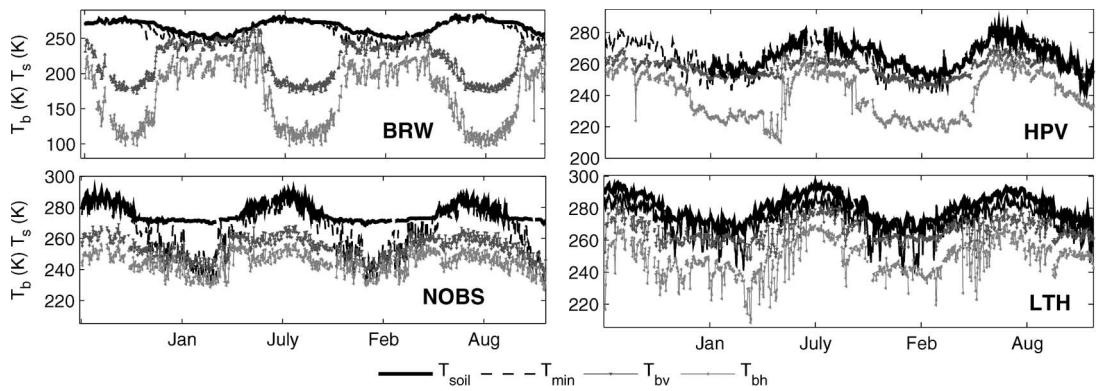

Fig. 3. AMSR-E 6.9-GHz V- and H-polarized brightness temperatures over selected study sites from 2002 to 2004.

V-polarization is less influenced by soil moisture, open water, and scattering.

The correlation between T_b and shallow ($<$ 20 cm) soil temperatures was greater than 0.75 for all AMSR-E spectral bands for sites without significant open water, as defined from the MODIS land cover windows. The higher frequencies (23.8–89 GHz) were well correlated ($r \geq 0.70$; $P < 0.001$) with *in situ* temperature observations for all soil depths ≤ 22 cm in both forested and nonforested sites. The highest correlations were observed at the 89-GHz band, which was somewhat surprising considering expected greater sensitivity to the atmosphere; however, precipitable water and cloud liquid water content influence atmospheric opacity and emission at 89 GHz and also tend to be correlated with surface temperature and tropospheric lapse rates. A similar analysis was conducted over Finland [15] and found that the 85-GHz channel from the SSM/I showed lower correspondence with surface temperature relative to 37 GHz. The AMSR-E lower frequencies ($\leq$ 18.7 GHz) showed significant but generally lower correspondence ($r \geq 0.65$; $P < 0.001$) with air and soil temperatures for all sites.

In nonforested locations [Fig. 2(a) and (b)], the AMSR-E brightness temperatures showed greater correspondence to shallow ($<$ 20 cm) soil temperatures $(r = 0.80{-}0.91)$ than minimum daily air temperatures $(r = 0.65{-}0.85)$; however, in forested locations [Fig. 2(c) and (d)], the brightness temperatures corresponded more closely to minimum daily air temperatures $(r = 0.91{-}0.95)$ than soil temperatures $(r = 0.75{-}0.90)$. Differences in T_b correlations with minimum air temperatures measured above and below the OAS forest canopy were small, whereas both were greater than correlations with site soil temperatures. The greater correspondence between T_b and air temperatures is due to the larger vegetation contribution to bulk surface microwave emission at the forested sites and soil temperatures insulated from below canopy air temperatures by additional leaf litter and a thicker humus layer.

Sites such as BRW, with a relatively large proportion of open water within the sensor footprint, showed a negative correlation between T_b and surface temperatures. The response was attributed to emissivity reductions from surface water. An increase in surface temperature leads to a decrease in T_b, where ice is melted to form liquid water. This precludes the use of a time-invariant emissivity parameter, particularly over sites with soil moisture variability and open water [19]. Open water also increases polarization ratio most strongly at lower frequencies, as indicated by the seasonal fluctuation of open water surface at BRW (Fig. 3), whereas over vegetation, such as grassland at LTH, the difference between H and V brightness temperatures shows a decreasing trend during the growing season, which is possibly the result of an increase in the depolarizing properties of a developing leaf canopy (Fig. 3). The polarization difference thereby provides a way in which the emissivity can be corrected for open water and soil moisture, but the influence of absorption and scattering by vegetation and winter snow layers over frozen ground must be taken into account.

III. Algorithm Formulation

A. Process-Based Approach

The aim of the process-based method is to reduce the dimensionality of the surface temperature problem by exploiting the expected frequency dependence of AMSR-E brightness temperatures T_b to geophysical variables influencing the surface emissivity. This approach uses empirical parameters describing the frequency dependence of geophysical parameters within simplified radiative transfer models. In addition to surface temperature, auxiliary parameters including vegetation water content/roughness equivalent and snow water equivalent are simultaneously produced. The method assumes that the retrieved surface temperature and auxiliary parameters represent linear spatial averages within the AMSR-E footprint.

The brightness temperature at polarization p (e.g., T_{bp}) of an object can be described as the product of the object's physical temperature T_s and its apparent emissivity e_p, i.e.,

$$T_{\mathrm{bp}} = e_p T_s. \tag{1}$$

Equation (1) is a simplified expression for a single vertically isothermal semi-infinite emitting layer. For nonisothermal conditions, the physical temperature can be defined as a weighted average across the emitting layer and the sensor field-of-view. The emissivity is related to the viewing angle and the complex dielectric constant, which varies with soil moisture for a smooth surface–atmosphere interface, by the Fresnel coefficients. The atmosphere influences T_{bp} in (1) by absorbing or scattering (in the case of precipitation) the emitted radiation

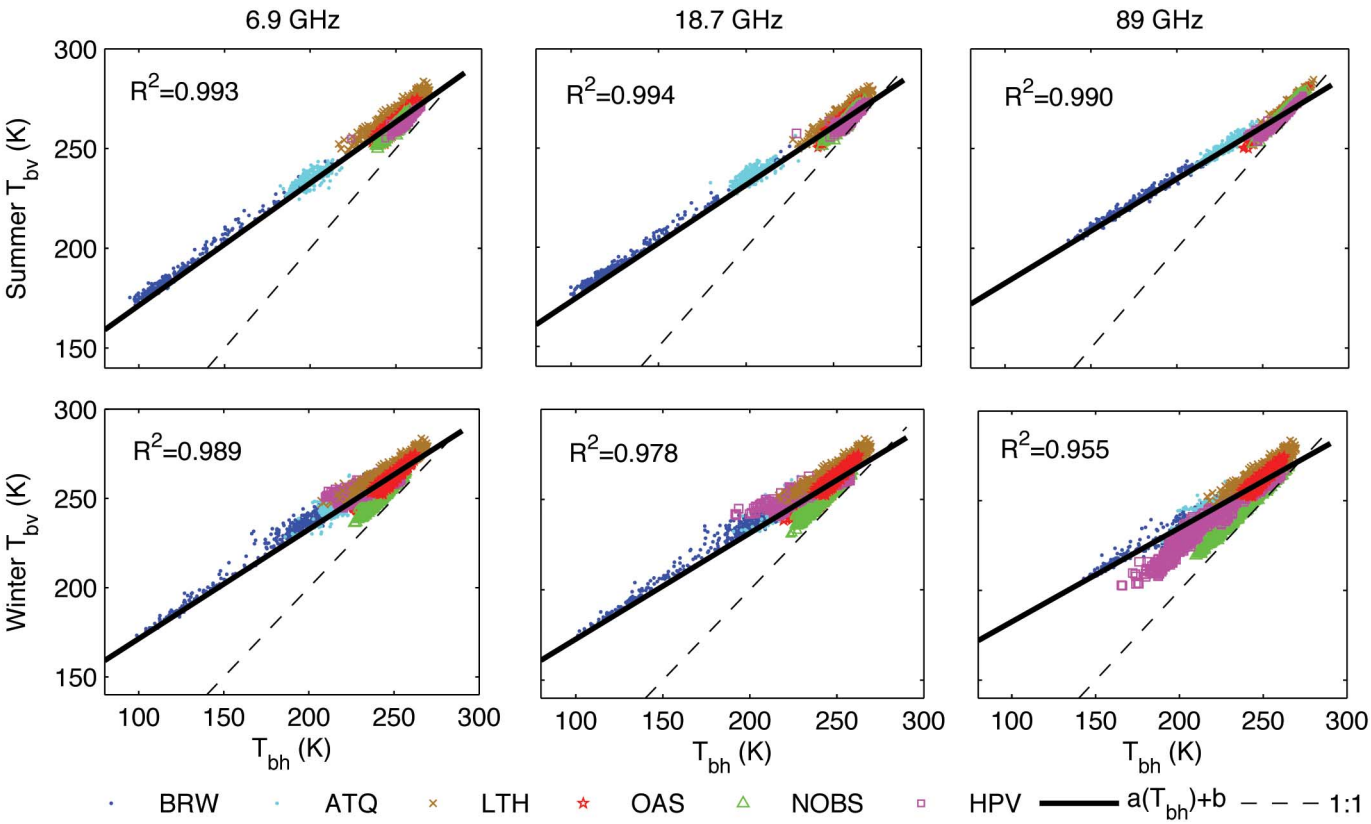

Fig. 4. Observed AMSR-E $T_{\rm bh}$ versus $T_{\rm bv}$ relations at the study sites. The R^2 statistic indicates the level of linear correlation between $T_{\rm bh}$ versus $T_{\rm bv}$ at BRW for each frequency. The black straight line represents the appropriate a and b parameters from Table III and the mean summer $T_{\rm soil}$ at BRW. The dashed straight line represents a 1 : 1 relationship.

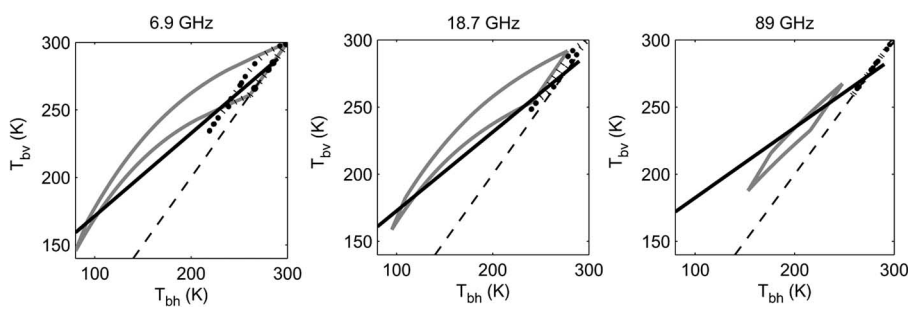

Fig. 5. Theoretical spectral dependence of $T_{\rm bh}$ and $T_{\rm bv}$ using the vegetation emission model represented by (5) in the absence of scaling effects. The region bounded by the curved lines marks the expected location of data points for $T_s = 261{-}300$ K, soil moisture $m_v = 1\%$ to 40%, and $g = 0$ (solid gray curves) and $g = 4$ kg/m^2 (dashed black curves). The black straight line represents the a and b parameters used to approximate (5) with scaling effects in the retrieval (6) and are equivalent to the black line in Fig. 4. The dashed line is the 1 : 1 line as in Fig. 4.

and contributing additional thermal emission. For simplicity, this investigation does not explicitly account for the influence of the atmosphere, under the assumption that changes in apparent surface emissivity generally have a much stronger influence than the atmosphere over the study region even at higher frequencies. The high correlation with observed soil temperatures and observations from a ground-based radiometer on the north slope of Alaska [43] indicates that this is a reasonable first-order assumption.

Apparent emissivities at H- and V-polarizations were linearly related by empirical parameters a and b across large areas at high latitudes [17], i.e.,

$$e_v = ae_h + b. \tag{2}$$

This relation was used for surface temperature and water fraction retrieval in sub-Arctic areas [17]. Similarly, AMSR-E T_b observations over our sites similarly show a linear trend (Fig. 4). Expressed in terms of surface temperature T_s, (2) becomes

$$T_{\rm bv} = aT_{\rm bh} + bT_s. \tag{3}$$

The Fresnel coefficients show a nonlinear relation between e_h and e_v with changes in the surface dielectric constant (Fig. 5). In atmospheric window channels, one would expect $T_{\rm bh}$ and $T_{\rm bv}$ to also closely follow this relation for specular flat homogenous surfaces. However, most terrestrial satellite pixels represent heterogeneous mixtures of emissivities that change

TABLE III
CONSTANT PARAMETERS CALIBRATED TO THE BRW SITE FOR THE PROCESS-BASED METHOD. THE α VALUES WERE OBTAINED USING A FREQUENCY POWER RELATION [25]. THE VALUES FOR a AND b ARE ALSO GIVEN FOR FROZEN CONDITIONS ($A_{\rm sn}$ AND $B_{\rm sn}$)

	Model Parameters				
Band (GHz)	***a***	***b***	a_{sn}	b_{sn}	α
6.9	0.631	0.402	0.592	0.450	0.486
10.7	0.607	0.416	0.574	0.468	0.566
18.7	0.601	0.418	0.578	0.466	0.688
23.8	0.557	0.453	0.523	0.508	0.749
36.5	0.554	0.455	0.526	0.506	0.87
89	0.518	0.481	0.508	0.515	1.188

over time and therefore produce linear trends between $T_{\rm bh}$ and $T_{\rm bv}$ among pixels and over time within each pixel [44]. This is because each satellite footprint represents a weighted average of the emissivities composing it, and the emissivities of each land cover fraction have a probability distribution that shifts over time. In Arctic regions during summer, this means that e_h and e_v will vary linearly between the emissivity of open water (approximately 0.57 for pure water at 20 °C observed at 6.9-GHz V-polarization) to that of dense vegetation over dry soil (approaching unity at V-polarization and slightly less than unity at H-polarization). A linear trend can therefore be fit to effective e_h and e_v data scatters to describe the expected change in emissivity with changes in the difference between observed $T_{\rm bh}$ and $T_{\rm bv}$. BRW was used as a calibration site for a and b over quasi-specular surfaces, due to locally large swings in emissivity in response to the annual cycle of sea ice formation and retreat occurring within the BRW tower window. Although BRW is not an ideal calibration location because it contains some vegetation during summer and some snow during winter, the large amount of open water and relatively shallow snow pack reduces the overall impact of vegetation and snow on the calibration. During winter, the slope a of the calibrated H–V relation decreased relative to its summer value, whereas the intercept b increased relative to its summer value at sites with little vegetation.

An examination of T_b over the tower locations indicates that during both summer and winter, a and b have a dependence on vegetation density that appears to shift apparent a toward unity and b toward zero from their typical thawed condition values that are reported in Table III (Fig. 6). Whereas higher frequencies ($>$ 18.7 GHz) saturate quickly with even small amounts of vegetation, the lower bands ($\leq$ 18.7 GHz) have a greater sensitivity to surface dielectric constant and therefore have a greater dynamic range of response to an overlying layer masking the surface. Winter snow has a similar impact on the apparent e_h and e_v relation, but the influence increases with frequency due to volume scattering within the snow pack.

1) Vegetation Radiative Transfer: Assuming that the surface temperature is equivalent to the canopy temperature, T_b that is observed from a vegetated surface can be expressed as

$$T_{\rm bp} = T_s \left\{ e_{\rm sp} \exp(-\tau_c) + (1-\omega_p)\left[1-\exp(-\tau_c)\right] \times \left[1 + r_{\rm sp}\exp(-\tau_c)\right]\right\}. \quad (4)$$

The soil emissivity $e_{\rm sp}$ is equal to $1 - r_{\rm sp}$, where $r_{\rm sp}$ is the reflectivity. The vegetation transmittance τ_c accounts for

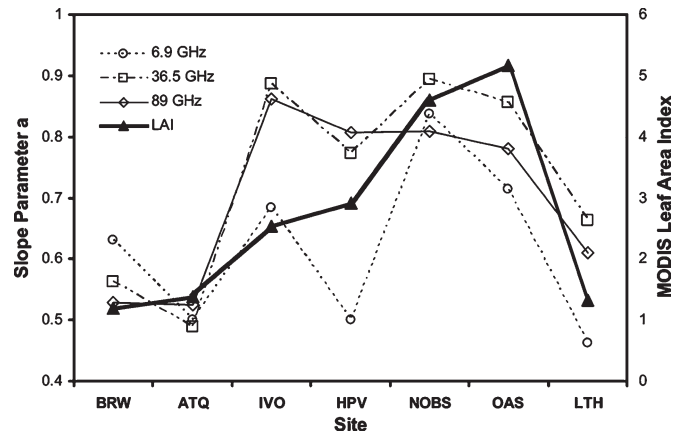

Fig. 6. Apparent slope parameter a derived by fitting (2) to the e_h versus e_v emissivity relation (2) at each site for each AMSR-E frequency. Maximum annual MODIS LAI for the dominant vegetation type is on the secondary y-axis.

the absorption of the upwelling signal by the canopy. The single scattering albedo ω_p accounts for radiation scattered by the canopy in the forward direction. Over dense vegetation, particularly at frequencies $>$ 18.7 GHz, the soil contribution becomes entirely masked, and (4) effectively reduces to $T_{\rm bp} = T_s(1-\omega_p)$ [45]. If ω_p is assumed to be negligible, (4) becomes [25]

$$T_{\rm bp} = T_s\left[1 - r_{\rm sp}\exp\left(-\alpha(f)g\right)\right] \quad (5)$$

where τ_c is rewritten in terms of a frequency-dependent parameter $\alpha(f)$ and a vegetation/roughness quantity g (in kilograms per square meter). Values for $\alpha(f)$ were determined by extending the exponential relationship presented in [25]. By inserting (5) into (3) and solving for the surface temperature, we arrive at

$$T_s = (T_{\rm bv} - aT_{\rm bh}) / \left[1 - a - \gamma + \exp(-\alpha g)(b - 1 + a + \gamma)\right]. \quad (6)$$

The empirical parameter γ is added to adjust the value of the denominator where the vegetation opacity becomes saturated. This parameter was set to a constant value of 0.012 and is added to partially account for extinction due to scattering and the exclusion in ω_p (4). As can be seen from (6) and (3), if the effect of vegetation is the same at both polarizations, the influence of vegetation is entirely by modifying the intercept b. This confirms that the apparent shift in the slope a with vegetation is caused by reduced sensitivity to the quasi-specular wet soil emission. The quantity g is an additional unknown and is determined using an iterative technique.

2) Snow Pack Radiative Transfer: The brightness temperature from a snow pack can be simply represented as a single scattering and attenuating layer, i.e.,

$$T_{\rm bp} = T_s\left[(1-\omega_{\rm sn})(1-\exp(-\tau_{\rm sn})) + e_{\rm sp}\exp(-\tau_{\rm sn})\right]. \quad (7)$$

The term $(1-\omega_{\rm sn})(1-\exp(-\tau_{\rm sn}))$ represents the thermal emission of the snow pack with single scattering albedo $(\omega_{\rm sn})$ and transmittance $(\tau_{\rm sn})$, whereas the term $e_{\rm sp}\exp(-\tau_{\rm sn})$ represents radiation emitted by the underlying frozen ground surface.

TABLE IV
COEFFICIENTS (STANDARD ERRORS) FIT TO THE MULTIBAND MULTIPLE-REGRESSION EQUATION IN (12)

All Sites	β_0	β_1	β_2	β_3	β_4	β_5
Thawed	74.792	0.915	-0.640	-0.927	1.42	230.553
	(4.743)	(0.122)	(0.208)	(0.189)	(0.093)	(9.217)
Frozen	246.905	0.913	-0.084	-2.618	1.892	-35.016
	(5.422)	(-0.159)	(0.240)	(0.187)	(0.093)	(8.338)

The physical temperature of the snow pack profile is assumed isothermal and equivalent in temperature to the underlying soil. The transmissivity and reflection at the snow pack interfaces, as well as multiple scattering, are assumed to be negligible. The snow pack transmittance can be represented by [46]

$$\tau_{\rm sn} = \exp\left(-b_{\rm sn} W \sec(\theta)/\lambda\right). \tag{8}$$

In (8), the parameter $b_{\rm sn}$ is set constant at 0.025, W represents the "water equivalent" of the snow pack (in centimeters), θ is the AMSR-E incidence angle, and λ is the free-space wavelength (in centimeters). W should be simply interpreted as a snow signal that includes the combined influence of snow pack water content, particle size, and total snow depth. As the purpose of this paper is surface temperature determination, an effort was not made to define W in terms of actual snow water equivalent, as in other studies [29]. By inserting (8) into (7) and combining with (6) and solving for surface temperature as in (6), the snow pack expression becomes

$$T_s = (T_{\rm bv} - aT_{\rm bh})/\left\{B + \exp(-\alpha g)[\exp(-\tau_{\rm sn}) \times [(1-a)(1-\omega_{\rm sn}) + b\,\exp(-\tau_{\rm sn})B]\right\} \tag{9}$$

where $B = 1 - a - \gamma$. Like g, the quantity W is an additional unknown and is determined using an iterative technique (8).

3) Iterative Solution for Surface Temperature: The radiative transfer equations (6) and (9) use a constrained 1-D iterative minimization technique to solve for one of the auxiliary quantities g and W with T_s while holding the other parameter (g or W) constant. The quantities g and W were bracketed within expected bounds (0–6 kg/m^2 and 0–10 cm, respectively). The physical temperature sensed by adjacent spectral bands is expected to be similar; thus, the weighted sum of squares of the pairwise differences between the surface temperature estimated between adjacent bands was used as the cost function Cf, i.e.,

$$Cf = \sum_{k=2}^{N} \left\{ \left[\hat{T}_s(k) - \hat{T}_s(k-1)\right] / \sigma(k) \right\}^2 \tag{10}$$

where $\hat{T}_s(k)$ denotes the surface temperature estimated at band $(k-1)$, and $\sigma(k)$ is the weight for the kth comparison summed over N bands. A golden section search with parabolic interpolation was used to minimize Cf. Surface temperature estimated at each frequency minimized Cf, and the quantities g and W were produced.

B. Multiple-Regression Approach

We employ a second empirical multiple-regression approach for comparison against the previous process-based method. This method follows the common practice of fitting multiple regression coefficients to several T_b channels and to index variables derived from those channels, such as the polarization difference ratio ξ [13]–[16] is defined as

$$\zeta = (T_{\rm bv} - T_{\rm bh})/(T_{\rm bv} + T_{\rm bh}). \tag{11}$$

Several frequencies and both H- and V-polarizations were used to account for changing surface conditions that differentially affect the emissivity at each channel. Index variables, such as ζ and channel differences, can be further used to reduce the number of parameters that must be fit [14]. Similar results can be obtained by incorporating H-polarization brightness temperatures in lieu of ζ. An advantage of this approach is that information from several channels can be exploited without more complicated physical derivations or numerical techniques. A disadvantage of this approach is that it does not provide more explicit information on surface conditions impacting the retrieval and largely depends on trial and error for algorithm improvement.

The multiple-regression algorithm was developed by stepwise forward selection on a full frequency set containing all bands of the V-polarized brightness temperatures and ζ values for each band, as it was determined that the V-polarized brightness temperatures alone could not well account for surface wetness. The resulting equation was chosen when the root-mean-square error (RMSE) of the estimate was not reduced by more than 0.5 K and the R^2 did not change significantly with the addition of another parameter. The stepwise regression yielded the following equation:

$$T_s = \beta_0 + \beta_1 T_{\rm bv6} + \beta_2 T_{\rm bv10} + \beta_3 T_{\rm bv23} + \beta_4 T_{\rm bv89} + \beta_5 \zeta_{89} \tag{12}$$

where the β's are the regression coefficients and are tabulated in Table IV. Separate coefficients were developed for thawed versus frozen conditions. The initial model fit to the training data resulted in $R^2 = 0.77$ and RMSE $= 2.84$ K for thawed conditions and $R^2 = 0.46$ and RMSE $= 4.93$ K for frozen conditions.

The freeze–thaw transition was identified through a change detection analysis of large (5–15 K) shifts in the AMSR-E T_b time series, which were most pronounced at wet tundra sites. Other satellite microwave remote sensing studies have shown similar temporal behavior in microwave backscatter and emission coinciding with temporal changes in land surface dielectric properties such as the landscape transitions between predominantly frozen and thawed conditions [47]–[49]. This dynamic response is driven primarily by the distinct increase in the bulk soil complex dielectric constant as water transitions between solid and liquid phases, causing a jump from high

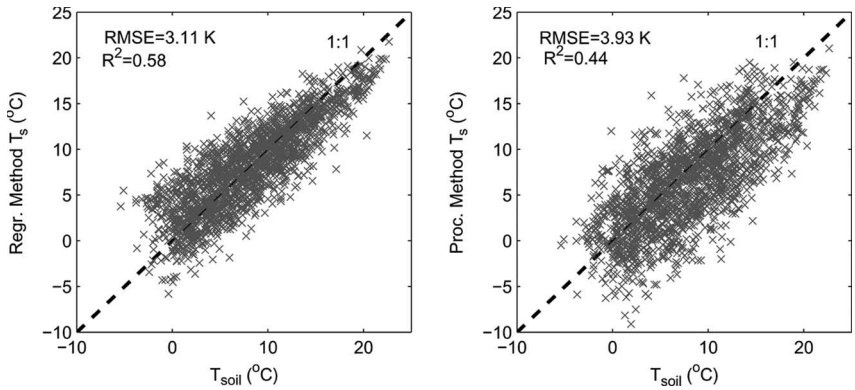

Fig. 7. Scatter plot of 2004 thawed season retrievals for the regression and process-based AMSR-E T_s methods and associated statistics.

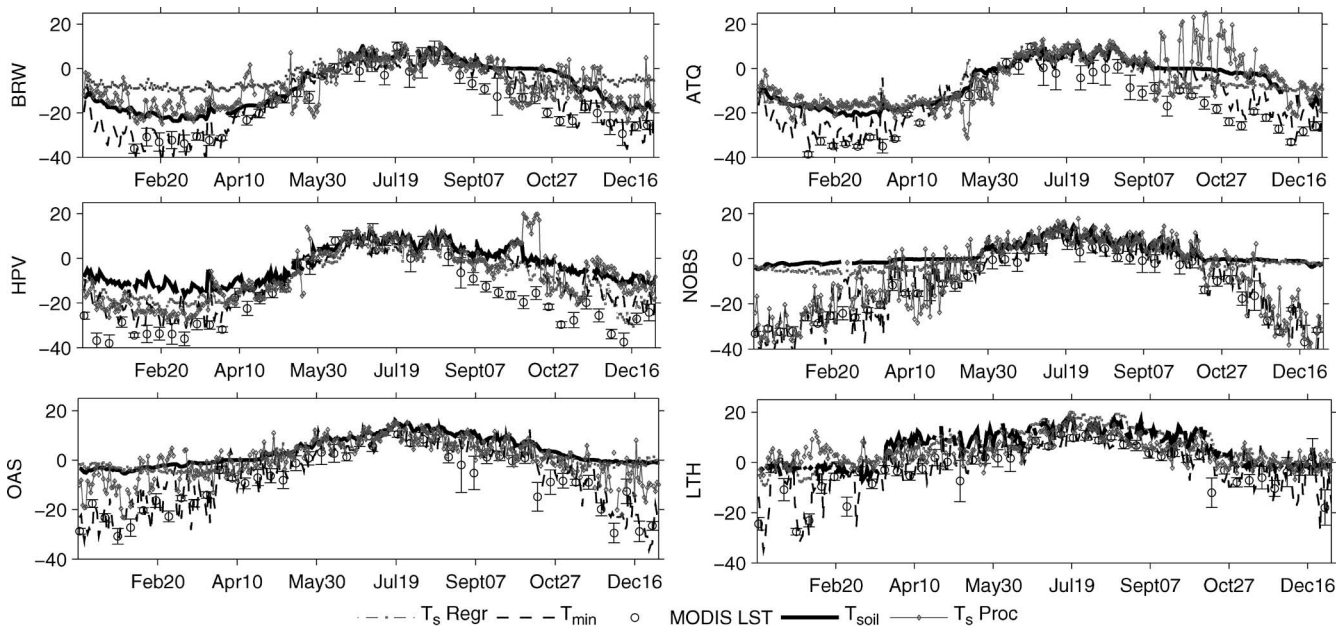

Fig. 8. Both methods of AMSR-E T_s retrievals (in degrees Celsius) plotted against $T_{\rm soil}$, $T_{\rm min}$, and MODIS LST at the study sites for 2004. MODIS LST error bars represent the standard deviation of the 1-km resolution-based MODIS LST results within a 60-km window centered at each site.

to low emissivity that decreases both H- and V-polarized T_b while increasing the polarization ratio, particularly at the lowest frequencies ($<$ 36.5 GHz), a response that dominates the T_b signal for wet cold lands [27]. An accurate freeze–thaw classification can be readily automated by applying the methods developed by McDonald *et al.* [26], although for this investigation, we identified seasonal freeze–thaw transitions through visual inspection of the AMSR-E time series data for each site to account for this source of variability in the method comparison.

C. Methods of Comparison

The *in situ* soil temperature data and corresponding daily T_b values were divided into a set for developing algorithm parameters and test set for evaluating algorithm performance. Days with missing soil or brightness temperature data were omitted from the analysis (10.8% of the entire test set). The ATQ and IVO sites had relatively short-duration data sets; thus, these whole data sets were included in only the test phase, whereas for the other sites, the entire year 2004 was set aside for algorithm testing. The remaining data for years 2002 and 2003 for five of the seven sites were used for fitting algorithm parameters. Daily AMSR-E soil temperature T_s retrievals for both retrieval methods under frozen and thawed conditions were compared to the daily minimum soil $T_{\rm soil}$ and air temperatures $T_{\rm min}$. Additionally, MODIS Aqua nighttime LST [50] 1-km resolution grid subsets [41] were extracted from ~60-km windows centered at each tower site corresponding to the AMSR-E L2A spatial resolution. Since MODIS and AMSR-E are both located on Aqua, they have essentially coincident observation times. The mean and standard deviation of the 1-km resolution, eight-day MODIS LST results were determined within each 60-km tower window and used as a surrogate measure of subgrid-scale temperature variability for the corresponding AMSR-E microwave-based temperature retrievals.

IV. Surface Temperature Retrieval

Figs. 7 and 8 show the results of the AMSR-E surface temperature retrievals at the tower locations. The corresponding statistical results are summarized in Tables V and VI. Both methods are generally able to capture the annual cycles and

TABLE V
THAWED CONDITION VALIDATION STATISTICS BY SITE FOR AMSR-E SURFACE TEMPERATURE METHODS. THE NUMBERS REPRESENT COMPARISON OF RETRIEVED T_s VERSUS T_{soil} ($T_{\min}$). R^2, COEFFICIENT OF DETERMINATION; RMSE, ROOT-MEAN-SQUARE ERROR; MAE, MEAN ABSOLUTE ERROR; MR, MEAN RESIDUAL (OBSERVED MINUS RETRIEVED); n, SAMPLE SIZE

	Process-Based Method				Regression Method				
SITE	**RMSE**	**R^2**	**MAE**	**MR**	**RMSE**	**R^2**	**MAE**	**MR**	***n***
BRW	2.96	0.45	2.40	1.12	2.57	0.59	2.14	0.86	105
	(3.91)	(0.23)	(3.27)	(-1.59)	(3.47)	(0.45)	(2.85)	(-1.88)	(120)
ATQ	2.22	0.69	1.83	-1.19	2.16	0.69	1.75	-0.94	99
	(3.74)	(0.41)	(2.90)	(-2.53)	(3.55)	(0.44)	(2.84)	(-2.31)	(100)
IVO	2.94	0.61	2.43	-1.70	4.032	0.75	3.85	-3.71	56
	(4.06)	(0.19)	(3.43)	(-1.10)	(4.58)	(0.22)	(3.92)	(-3.40)	(102)
HPV	3.15	0.77	2.69	-2.39	4.99	0.76	4.54	-4.43	90
	(3.84)	(0.36)	(3.09)	(-1.93)	(4.69)	(0.46)	(4.11)	(-3.97)	(90)
NOBS	3.72	0.32	2.91	-0.59	3.00	0.37	2.43	-0.35	132
	(5.74)	(0.30)	(4.60)	(-3.77)	(5.47)	(0.30)	(4.05)	(-3.53)	(132)
OAS	3.99	0.60	3.22	2.57	2.71	0.62	2.16	1.05	186
	(4.81)	(0.44)	(3.85)	(-1.68)	(5.18)	(0.44)	(4.32)	(-3.20)	(186)
LTH	5.55	0.68	4.86	4.72	2.84	0.65	2.32	0.30	187
	(5.12)	(0.44)	(4.16)	(-2.61)	(8.30)	(0.41)	(7.32)	(-7.03)	(187)

TABLE VI
FROZEN CONDITION VALIDATION STATISTICS BY SITE FOR AMSR-E SURFACE TEMPERATURE METHODS. THE NUMBERS REPRESENT COMPARISON OF RETRIEVED T_s VERSUS T_{soil} ($T_{\min}$). R^2, COEFFICIENT OF DETERMINATION; RMSE, ROOT-MEAN-SQUARE ERROR; MAE, MEAN ABSOLUTE ERROR; MR, MEAN RESIDUAL (OBSERVED MINUS RETRIEVED); n, SAMPLE SIZE

	Process-Based Method				Regression Method				
SITE	**RMSE**	**R^2**	**MAE**	**MR**	**RMSE**	**R^2**	**MAE**	**MR**	***n***
BRW	7.00	0.24	5.32	-0.91	8.67	0.35	7.86	-6.17	222
	(12.52)	(0.25)	(11.05)	(-.891)	(16.31)	(0.42)	(14.11)	(-13.78)	(241)
ATQ	7.85	0.51	5.65	-1.24	4.95	0.70	4.05	2.54	247
	(13.25)	(0.21	(11.32)	(-7.24)	(7.80)	(0.63)	(6.40)	(-3.80)	(262)
IVO	10.51	0.49	9.24	5.77	6.18	0.64	5.23	5.11	205
	(10.48)	(0.42)	(7.67)	(-5.92)	(7.54)	(0.71)	(6.10)	(-4.66)	(252)
HPV	9.23	0.48	6.83	-2.71	5.53	0.50	4.32	-3.36	228
	(11.05)	(0.54)	(9.02)	(-8.17)	(7.06)	(0.66)	(5.86)	(-4.68)	(222)
NOBS	19.48	0.48	16.29	15.44	3.11	0.14	2.60	2.32	196
	(7.96)	(0.68)	(6.21)	(-3.07)	(20.35)	(0.04)	(16.88)	(-16.34)	(202)
OAS	7.42	0.22	5.96	4.47	3.06	0.03	2.51	1.83	145
	(13.38)	(0.30)	(11.36)	(-0.87)	(16.78)	(0.06)	(14.45)	(-13.45)	(145)
LTH	4.76	0.00	3.57	-1.61	3.37	0.36	2.96	2.01	124
	(12.83)	(0.02)	(9.70)	(-8.78)	(10.56)	(0.13)	(7.74)	(-5.16)	(124)

daily variability of soil and air temperatures at each site. More favorable results are obtained during the summer thawed season relative to winter frozen conditions. The use of 89 GHz in estimating T_s did not degrade the retrievals in either of the AMSR-E T_s methods. The T_s results for the process-based method for each frequency were nearly equivalent, where the value of Cf was low.

Several instances of either systematic bias or anomalous short-term spikes or dips in AMSR-E-retrieved T_s are worthy of detailed discussion. Correspondence of AMSR-E T_s with T_{soil} and $T_{\min}$ varied among sites, as the latitudinal range of the sites presented different soil-to-air temperature gradients at each location. Subpixel spatial heterogeneity was also a significant factor for the microwave T_s retrievals. The freeze–thaw transition and snow during the winter season significantly impacted winter retrievals. Land cover characteristics, such as open water and vegetation phenology, presented a range of temporally dynamic and spatially variant emissivities within and among sites. The accuracy of the temperature retrievals under these conditions indicates the skill of the retrieval method to account for these dynamic effects.

A. Comparison to In Situ Air and Soil Temperatures and MODIS LST

The process-based approach obtained lower errors at the Arctic sites relative to the boreal locations, with the exception of HPV (RMSE < 3 °C versus RMSE > 3 °C; Table V). This demonstrates that the model correctly accounts for changes in surface emissivity in response to open water surfaces, which dominate regional land cover conditions at higher latitudes. The regression method also performed well over the Arctic tundra sites but had higher error at HPV. The somewhat poorer performance of both methods for HPV relative to IVO, another tussock tundra site, can be partially attributed to erroneous predictions during the freeze–thaw transition, which were more severe at HPV and partially attributed to a greater fractional coverage of tussock tundra at HPV (97% open shrubland and 1% barren ground versus 82% open shrubland and 13% barren ground at IVO). For both the IVO and HPV tussock sites, the regression method consistently overpredicted T_s [mean residual (MR) $= -3.71$ K and -4.43 K, respectively]. The overestimation at the tussock sites was therefore attributed to ζ, similar to forested sites, but the thermal gradient between soil and canopy temperatures was much different than forested sites, as shown in Section II and Fig. 2. IVO and HPV have ζ that was more similar to the boreal forest sites than to the grassland site LTH despite the short stature tussock tundra vegetation. The summer minimum ζ at 6.9 GHz varied from 0.0107 at IVO, 0.0099 at HPV, 0.0112 at NOBS, and 0.0149 at LTH. Anisotropy of tussock tundra has previously been noted in [51]. The regression method had generally less bias over the boreal sites relative to the process-based method. Much of the bias can be explained by the near-surface soil-to-air temperature gradient.

Summer soil temperature observations at the high-latitude Arctic sites were only slightly higher than the daily minimum air temperatures. These daily temperature differences increased for lower latitude boreal locations, with the greatest average difference of about 5 °C occurring during mid-summer conditions at LTH. Maximum daily differences between T_{soil} and T_{min} decreased with increasing latitude and ranged from 24 °C for LTH to 9.65 °C at BRW. These differences reflect stronger surface heating and larger diurnal temperature gradients at drier, lower latitude locations; these conditions impact the soil temperature comparisons by increasing surface temperature spatial and vertical heterogeneity, and decreasing the correspondence between relatively coarse-scale AMSR-E-based T_s and *in situ* soil temperature measurements. In contrast, reduced solar irradiance at higher latitudes and the relatively large heat capacity of water and enhanced latent energy transfer in areas with large amounts of surface water moderates T_{min} and T_{soil} differences for tundra sites. As a result, the AMSR-E process-based retrieval method underpredicted soil temperatures at OAS and LTH relative to *in situ* measurements (Table V). The bias is removed or reversed when the retrieval is compared to T_{min} (Table V), indicating the bias was mostly the result of the near-surface soil-to-air temperature gradient and not assumptions in the vegetation model. The underprediction was greatest with the process-based approach relative to the regression method because the coefficients of the regression approach were tuned to the soil temperature when the equation coefficients were established.

The relatively coarse-scale AMSR-E results from the two approaches are in general agreement with the footprint mean LST derived from MODIS. MODIS LST shows that mean surface skin temperatures within the AMSR-E field-of-view generally correspond more closely to T_{min} rather than to soil temperature, due to the descending (morning) overpass time and shallow penetration depth. At the tundra locations (BRW, ATQ, and HPV), MODIS LST shows generally colder temperatures relative to T_{min} and both AMSR-E T_s methods. The standard deviation of the LST within each pixel ranges from < 1 °C in winter to 11 °C during the fall freeze–thaw transition. Summer season LST pixel standard deviations are $\sim$3.6 °C at the Arctic sites and $\sim$2.7 °C at the boreal sites. These values suggest that LST spatial heterogeneity within the tower windows is on the order of the AMSR-E-based temperature accuracy determined from pixel-to-point comparisons with *in situ* observations during the thawed season.

B. Winter Retrievals and the Freeze–Thaw Transition

The onset of winter induces rapid changes in surface dielectric properties during the transition to frozen conditions. Soil-to-air temperature gradients and the accumulation of a scattering snow pack are also important factors. It is therefore not surprising that the AMSR-E-based temperature retrievals significantly degrade during the winter months. A marked increase in retrieval error during freeze–thaw transitions was evident for the process-based method (Fig. 7). This error was more severe during fall than in spring because the seasonal thaw transition generally occurred rapidly, whereas the transition to seasonal frozen conditions was more gradual, with multiple freeze–thaw events occurring over a relatively long duration. The erroneously high temperature retrievals between late September and early October at ATQ and HPV indicate that this effect is strongest at tundra sites (Fig. 8). The relatively simplistic freeze–thaw classification approach used for this investigation does not account for spatial heterogeneity or multiple freeze–thaw events occurring within the sensor footprint. Also, freeze–thaw state varies within each $\sim$60-km microwave footprint during the transition. An earlier study on the north slope of Alaska compared tower-based 37 GHz brightness temperatures and SSM/I observations, concluding that the satellite- and ground-observed brightness temperatures differ as a result of spatial heterogeneity in landscape dielectric properties during the seasonal freeze–thaw transition [43].

Snow cover impacts the AMSR-E temperature retrievals of both methods by insulating soil temperatures. As can be seen in Fig. 8, the AMSR-E temperature retrievals correspond more closely to minimum daily air temperatures and MODIS LSTs than soil temperatures for sites under seasonal snow cover for the process-based approach. A similar pattern is evident at NOBS, where soil temperatures fluctuate near 0.0 °C, whereas air temperatures range to as low as -40 °C. The positive bias relative to *in situ* temperature measurements at BRW (MR $= -6.60$ °C; Table VI) is also the result of the regression equation representing an insulating snow pack that was present at most of the other sites (Fig. 8).

C. Evaluation of Auxiliary Parameters From the Process-Based Method

The accuracy of the process-based T_s retrieval under temporally dynamic surface conditions indicates the skill of the method to account for the effects of changing emissivities. The assumption of a linear relation between T_{bh} and T_{bv} accounts for changes in surface dielectric constant. As stated earlier, this relationship is related to the scale of the microwave observations over quasi-specular surfaces and appears to shift with surface freeze–thaw state. Earlier studies have used this relation for surface temperature retrieval at both site [29] and regional scales [17]; however, the impact of the absorption of quasi-specular surface emissions by vegetation and volume scattering within snow pack required the use of simple radiative transfer equations to describe the behavior of the polarization difference over these surfaces. In addition to surface temperature, the inversion of these equations enabled the retrieval of canopy water content/roughness equivalent g and a snow water equivalent parameter W.

The results for the g parameter are given in Fig. 9 and indicate that g corresponds closely with variations in the eight-day MODIS leaf area index (LAI) among the sites, as well as the seasonal trends at each site for 2003. One anomalous spike in g at ATQ in 2003 (Fig. 9) during the fall freeze is similar to such a spike in 2004, causing overprediction of T_s during the fall freeze (Fig. 8). The influence of g is to modify the b parameter in (2), increasing the predicted surface temperature. The surface temperature prediction at 6.9 GHz is most sensitive to the influence of g because this band is most sensitive to surface water and thus will have a greater relative response to the masking of the underlying surface, whereas the 89-GHz

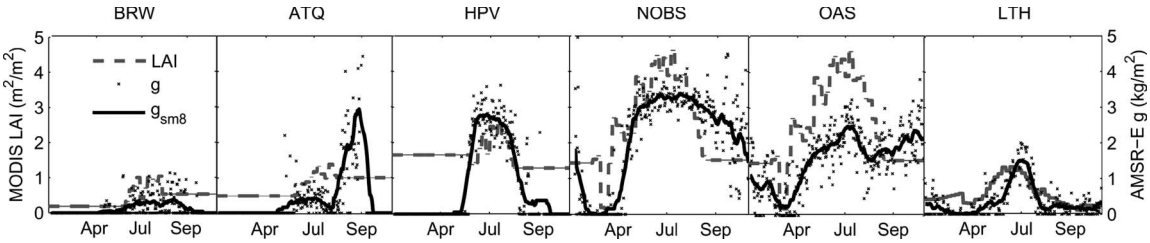

Fig. 9. MODIS eight-day LAI (in square meters per square meter) time series and AMSR-E auxiliary g (in kilograms per square meter) vegetation/roughness parameter results for 2003. The points represent daily values of g, whereas the solid black lines represent an eight-day running average (g_{sm8}).

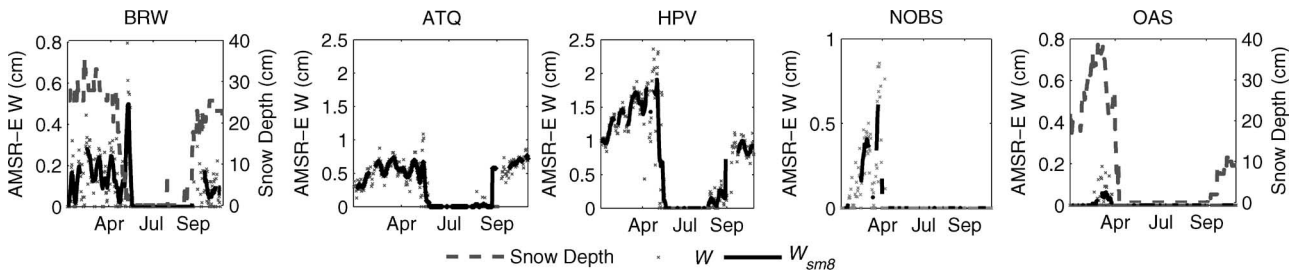

Fig. 10. Snow depth at BRW and OAS (dashed gray lines) and AMSR-E auxiliary W (in centimeters). The points represent daily values of W, whereas the solid black lines represent an eight-day running average.

band saturates quickly with even a small amount of vegetation. The best T_s results were obtained by employing all bands equally weighted in the iterative minimization. When only the highest frequency bands (18.7–89 GHz) were included, T_s was overpredicted, and retrieved values of g approached 6 kg/m^2 at NOBS, which was assumed unreasonable for boreal forest given the results of [15]. Similarly, when only the lowest bands (18.7 GHz and less) were included, T_s was underpredicted. The inclusion of a more detailed radiative transfer equation, such as (3), may further improve results by accounting for scattering effects. However, the surface temperature results of this investigation show that bias introduced by scattering within the vegetation canopy is a relatively small factor and can be mitigated with the empirical parameter γ.

In contrast to a vegetation canopy, scattering is the main effect of snow cover on the linear relation between T_{bh} and T_{bv}. Scattering decreases the T_s estimates from (6) more strongly at higher frequencies relative to lower frequencies, which is the opposite spectral effect of vegetation absorption. This poses a difficulty for the current algorithm, where vegetation persists above the snow pack in winter, such as the boreal forest at NOBS and OAS (Fig. 10). The opposing effects of vegetation and snow on predicted T_s cause g to unreasonably decline to zero during the winter at the NOBS evergreen forest site and gives an unreasonably low estimate of W, rising only above zero when the snow pack scattering spectral signal is strong enough to overwhelm the vegetation absorbance spectral signature. This pattern is also evident at the OAS site, where W rises only briefly above zero, corresponding to the peak depth of the *in situ* snow pack measurement. Some of the error in the process-based winter T_s retrieval can be attributed to this effect because minimizing Cf cannot arrive at unbiased T_s estimate when a portion of the spectral signature is confounded by the vegetation effect.

Snow packs also vary greatly in their physical characteristics [29], and the simplistic treatment in this paper cannot account for changes in snow grain size, the formation of ice lenses and associated impacts on the extinction and scattering coefficients influencing ω_{sn} and b_{sn}, which were held constant in this investigation. However, the radiative transfer treatment of the snow pack did produce a clear snow signal (Fig. 10). We lacked ground data on snow for most sites in this paper, with the exception of BRW and OAS; however, the snow signal shows the expected seasonal pattern, accumulating throughout the season and peaking before a rapid decline in spring.

V. Conclusion

The seasonal dynamics of multifrequency AMSR-E T_b observations and their correlation with near-surface soil and air profile temperatures at high latitude sites were evaluated. The results demonstrate that brightness temperatures were highly correlated $(r > 0.85)$ with minimum daily air temperatures at forested locations and better correlated with soil temperatures $(r > 0.80)$ than with minimum daily air temperatures at nonforested locations, with the highest correlation at frequencies $>$ 18.7 GHz. The linear correlation of T_b with surface temperatures was lower at sites with low vegetation and high soil moisture variability, such as the LTH grassland location, and the linear correlation was completely decoupled at sites with a large fraction of open water. These results indicate that sensing depth can vary significantly among land covers; changes in emissivity due to open water, soil moisture, and depolarization from vegetation density are important factors; and T_b observations maintain high correlation with surface temperature at high latitudes under most common conditions without explicit atmospheric corrections.

Two methods to retrieve soil temperatures in boreal and Arctic landscapes from the AMSR-E sensor were developed and compared to *in situ* soil temperatures at biophysical network sites. The regression method had lower overall error $(\mathrm{RMSE} = 3.11\ \mathrm{K})$ than the process-based method

(RMSE = 3.93 K), although performance was quite variable between sites. Algorithm performance was primarily influenced by: 1) the vertical gradient between near-surface T_{soil} and T_{min}, which caused RMSE $>$ 3 K for the process-based method at the boreal sites and consistent bias offset of up to 4 K in the regression method at the tussock tundra locations; 2) subgrid-scale surface temperature heterogeneity within the AMSR-E footprint represented by MODIS LST standard deviations, which could be as much as 11 K in the fall freeze–thaw transitions; 3) large fluctuations in surface dielectric properties during freeze–thaw state transitions, particularly in the fall, and the insulating and scattering influence of the winter-time snow pack greatly increased error (RMSE increased by $>$ 4 K) during frozen periods; and 4) the accurate determination of model constants and skill of algorithm parameters to represent variable surface conditions and dynamic surface microwave emission.

Our results suggest that atmospheric effects on passive microwave measurements over high-latitude regions are less important for soil temperature estimation than seasonal and spatial variability in surface emissivity; however, the improved treatment of atmospheric effects would likely further improve results in future applications. Future work is needed to refine the frequency-dependent effects of vegetation and seasonal snow cover, to include more detailed radiative transfer equations, and to continue to develop a dynamic freeze–thaw classification. The soil temperature retrieval methods in this investigation are appropriate for biophysical modeling activities in Arctic and boreal regions. Furthermore, the iterative technique presented in this paper and the associated auxiliary quantities will be germane to other microwave-based land surface geophysical parameter retrieval studies.

ACKNOWLEDGMENT

The authors would like to thank F. A. Heinsch of the Numerical Terradynamic Simulation Group for obtaining and processing tower station data, and Ameriflux, FLUXNET Canada, and CALM site principal investigators and their teams for the diligent collection of field data and generously allowing the authors to use it for this study. These investigators include: W. C. Oechel and the Global Change Research Group of San Diego State University (Barrow, Atqasuk, and Ivotuk); L. Hinzman and D. Kane (University of Alaska Fairbanks) (Happy Valley/Sagwon Hill site); A. Dunn and S. Wofsy of Harvard University (BOREAS NSA Old Black Spruce); T. A. Black of the University of British Columbia (BOREAS SSA Old Aspen); and L. Flanagan of the University of Lethbridge (Lethbridge). The authors would also like to thank three anonymous reviewers for helpful comments that significantly improved this manuscript.

REFERENCES

[1] W. C. Oechel, S. J. Hastings, G. L. Vourlitis, M. Jenkins, G. Riechers, and N. Grulke, "Recent change of Arctic tundra ecosystems from a net carbon dioxide sink to a source," *Nature*, vol. 361, no. 6412, pp. 520–523, Feb. 1993.

[2] M. C. Serreze, J. E. Walsh, F. S. Chapin, T. Osterkamp, M. Dyurgerov, V. Romanovsky, W. C. Oechel, J. Morison, T. Zhang, and R. G. Barry, "Observational evidence of recent change in the northern high-latitude environment," *Clim. Change*, vol. 46, no. 1/2, pp. 159–207, 2000.

[3] L. D. Hinzman, N. D. Bettez, W. R. Bolton, F. S. Chapin, M. B. Dyurgerov, C. L. Fastie *et al.*, "Evidence and implications of recent climate change in northern Alaska and other Arctic regions," *Clim. Change*, vol. 72, no. 3, pp. 251–298, Oct. 2004.

[4] W. L. Gates, J. F. B. Mitchell, G. J. Boer, U. Cubasch, and V. P. Meleshko, "Climate modeling, climate prediction and model validation," in *Climate Change 1992: The Supplemental Report to the IPCC Scientific Assessment*, J. T. Houghton, B. A. Callander, and S. K. Varney, Eds. Cambridge, U.K.: Cambridge Univ. Press, 1992, pp. 97–135.

[5] J. Christensen, M. Hulme, H. Von Storch, P. Whetton, R. Jones, L. Mearns, and C. Fu, "Chapter 10: Regional climate information evaluation and projections," in *Climate Change 2001: The Scientific Basis*, J. T. Houghton, Y. Ding, D. J. Griggs, M. Noguer, P. J. van der Linden, X. Dai, K. Maskell, and C. A. Johnson, Eds. Cambridge, U.K.: Cambridge Univ. Press, 2001.

[6] L. D. Hinzman and D. L. Kane, "Potential response of an Arctic watershed during a period of global warming," *J. Geophys. Res.*, vol. 97, no. D3, pp. 2811–2820, 1992.

[7] F. A. Heinsch, M. Zhao, S. W. Running, J. S. Kimball, R. R. Nemani, K. J. Davis *et al.*, "Evaluation of remote sensing based terrestrial production from MODIS using AmeriFlux eddy tower flux network observations," *IEEE Trans. Geosci. Remote Sens.*, vol. 44, no. 7, pp. 1908–1925, Jul. 2006.

[8] L. L. Miller, K. M. Hinkel, F. E. Nelson, R. F. Paetzold, and S. I. Outcalt, "Spatial and temporal patterns of soil moisture and thaw depth at Barrow, Alaska USA," in *Proc. 7th Int. Permafrost Conf.*, A. G. Lewkowicz and M. Allard, Eds., Yellowknife, NT, Canada, Jun. 23–27, 1998, pp. 731–737, no. 57.

[9] A. D. McGuire, C. Wirth, M. Apps, J. Beringer, J. Clein, H. Epstein *et al.*, "Environmental variation, vegetation distribution, carbon dynamics and water/energy exchange at high latitudes," *J. Veg. Sci.*, vol. 13, no. 3, pp. 301–314, Jun. 2002.

[10] K. Goita, A. Royer, and N. Bussieres, "Characterization of land surface thermal structure from NOAA-AVHRR data over a northern ecosystem," *Remote Sens. Environ.*, vol. 60, no. 3, pp. 282–298, Jun. 1997.

[11] Z. Wan, Y. Zhang, Q. Zhang, and Z. Li, "Validation of the land-surface temperature products retrieved from Terra Moderate Resolution Imaging Spectroradiometer data," *Remote Sens. Environ.*, vol. 83, no. 1/2, pp. 163–180, Nov. 2002.

[12] J. C. Comiso, "Warming trends in the Arctic from clear sky satellite observations," *J. Climate*, vol. 16, no. 21, pp. 3498–3510, 2002.

[13] M. J. McFarland, R. L. Miller, and C. M. Neale, "Land surface temperature derived from the SSM/I passive microwave brightness temperatures," *IEEE Trans. Geosci. Remote Sens.*, vol. 28, no. 5, pp. 839–845, Sep. 1990.

[14] E. G. Njoku, "Surface temperature estimation over land using satellite microwave radiometry," in *Passive Microwave Remote Sensing of Land-Atmosphere Interactions*, B. J. Choudbury, Y. H. Kerr, E. G. Njoku, and P. Pampaloni, Eds. Utrecht, The Netherlands: VSP, 1995, pp. 509–530.

[15] J. T. Pulliainen, J. Grandell, and M. T. Hallikainen, "Retrieval of surface temperature in boreal forest zone from SSM/I data," *IEEE Trans. Geosci. Remote Sens.*, vol. 35, no. 5, pp. 1188–1200, Sep. 1997.

[16] A. Basist, N. C. Grody, T. C. Peterson, and C. N. Williams, "Using the special sensor microwave/imager to monitor land surface temperatures, wetness, and snow cover," *J. Appl. Meteorol.*, vol. 37, no. 9, pp. 888–911, Sep. 1998.

[17] M. Fily, A. Royer, K. Goita, and C. Prigent, "A simple retrieval method for land surface temperature and fraction of water surface determination from satellite microwave brightness temperatures in sub-Arctic areas," *Remote Sens. Environ.*, vol. 83, no. 3, pp. 328–338, May 2003.

[18] E. G. Njoku, P. Ashcroft, T. K. Chan, and L. Li, "Global survey and statistics of radio-frequency interference in AMSR-E land observations," *IEEE Trans. Geosci. Remote Sens.*, vol. 43, no. 5, pp. 938–947, May 2005.

[19] S. W. Ellingson and J. T. Johnson, "A polarimetric survey of radio-frequency interference in C- and X-Bands in the continental United States using WindSat radiometry," *IEEE Trans. Geosci. Remote Sens.*, vol. 44, no. 3, pp. 540–548, Mar. 2006.

[20] E. G. Njoku, T. J. Jackson, V. Lakshmi, T. K. Chan, and S. V. Nghiem, "Soil moisture retrieval from AMSR-E," *IEEE Trans. Geosci. Remote Sens.*, vol. 41, no. 2, pp. 215–229, Feb. 2003.

[21] M. Owe, R. de Jeu, and J. Walker, "A methodology for surface soil moisture and vegetation optical depth retrieval using the microwave polarization difference index," *IEEE Trans. Geosci. Remote Sens.*, vol. 39, no. 8, pp. 1643–1654, Aug. 2001.

[22] C. Prigent, F. Aires, W. B. Rossow, and A. Robock, "Sensitivity of satellite microwave and infrared observations to soil moisture at a global scale: Relationship of satellite observations to in situ soil

moisture measurements," *J. Geophys. Res.*, vol. 110, no. D07110, 2005. DOI:10.1029/2004JD005094.

[23] S. Paloscia and P. Pampaloni, "Microwave polarization index for monitoring vegetation growth," *IEEE Trans. Geosci. Remote Sens.*, vol. 26, no. 5, pp. 617–621, Sep. 1988.

[24] T. J. Jackson and T. J. Schmugge, "Vegetation effects on the microwave emission from soils," *Remote Sens. Environ.*, vol. 36, no. 3, pp. 203–212, Jun. 1991.

[25] E. G. Njoku and S. K. Chan, "Vegetation and surface roughness effects on AMSR-E land observations," *Remote Sens. Environ.*, vol. 100, no. 2, pp. 190–199, Jan. 2006.

[26] K. C. McDonald, J. S. Kimball, E. G. Njoku, R. Zimmerman, and M. Zhao, "Variability in springtime thaw in the terrestrial high latitudes: Monitoring a major control on the biospheric assimilation of atmospheric carbon dioxide with spaceborne microwave remote sensing," *Earth Interact.*, vol. 8, no. 20, pp. 1–23, 2004.

[27] K. C. McDonald and J. S. Kimball, "Chapter 53, Freeze–thaw states using both active and passive microwave sensors," in *Encyclopedia of Hydrological Sciences*, M. G. Anderson, Ed. Hoboken, NJ: Wiley, 2005.

[28] D. Hiltbrunner, C. Matzler, and A. Wiesmann, "Monitoring land surfaces with combined DMSP-SSM/I and ERS-1 scatterometer data," in *Proc. IGARSS Symp.*, Pasadena, CA, 1994, pp. 1945–1947.

[29] C. Matzler, "Passive microwave signatures of landscapes in winter," *Meteorol. Atmos. Phys.*, vol. 54, no. 1–4, pp. 241–260, Mar. 1994.

[30] F. Aires, C. Prigent, W. B. Rossow, and M. Rothstein, "A new neural network approach including first guess for retrieval of atmospheric water vapor, cloud liquid water path, surface temperature, and emissivities over land from satellite microwave observations," *J. Geophys. Res.*, vol. 106, no. D14, pp. 14 887–14 907, 2001.

[31] T. Boden, *Ameriflux*, Jun. 22, 2006. [Online]. Available: http://public.ornl.gov/ameriflux/index.html

[32] D. L. Kane and L. D. Hinzman. (2006, Oct. 12). *Climate Data From the North Slope Hydrology Research Project*, Univ. Alaska, Fairbanks, Water and Environ. Res. Center, Fairbanks, AK. [Online]. Available: http://www.uaf.edu/water/projects/NorthSlope/

[33] W. C. Oechel, G. L. Vourlitis, S. J. Hastings, R. C. Zulueta, L. Hinzman, and D. Kane, "Acclimation of ecosystem CO_2 exchange in the Alaskan Arctic in response to decadal climate warming," *Nature*, vol. 406, no. 6799, pp. 978–981, Aug. 2000.

[34] H. E. Epstein, M. P. Calef, M. D. Walker, F. S. Chapin, and A. M. Starfield, "Detecting changes in Arctic tundra plant communities in response to warming over decadal time scales," *Glob. Change Biol.*, vol. 10, no. 8, pp. 1325–1334, Aug. 2004.

[35] K. M. Hinkel and F. E. Nelson, "Spatial and temporal patterns of active layer thickness at Circumpolar Active Layer Monitoring (CALM) sites in northern Alaska, 1995–2000," *J. Geophys. Res.*, vol. 108, no. D2, pp. 8168–8181, 2003.

[36] A. L. Dunn and S. C. Wofsy, *Boreal Forest CO_2 Flux, Soil Temperature, and Meteorological Data*. Cambridge, MA: Dept. Earth & Planetary Sci., Harvard Univ., 2006.

[37] J. Griffis, T. A. Black, D. Gaumont-Guay, G. B. Drewitt, Z. Nesic, A. G. Barr, K. Morgenstem, and N. Kljun, "Seasonal variation and partitioning of ecosystem respiration in a southern boreal aspen forest," *Agric. For. Meteorol.*, vol. 125, no. 3/4, pp. 207–223, 2004.

[38] L. B. Flanagan and B. G. Johnson, "Interacting effects of temperature, soil moisture and plant biomass production on ecosystem respiration in a northern temperate grassland," *Agric. For. Meteorol.*, vol. 130, no. 3/4, pp. 237–253, 2005.

[39] E. G. Njoku, "AMSR land surface parameters," *ATBD 3.0*, 1999, Pasadena, CA: Jet Propulsion Lab. [Online]. Available: http://eospso.gsfc.nasa.gov/ftp_ATBD/REVIEW/AMSR/atbd-amsr-land.pdf

[40] P. Ashcroft and F. Wentz, "Algorithm theoretical basis document, AMSR level 2A algorithm," RSS, Santa Rosa, CA, RSS Tech. Rep. 121 599B-1, 1999.

[41] M. A. Friedl, D. K. McIver, J. C. F. Hodges, X. Y. Zhang, D. Muchoney, A. H. Strahler *et al.*, Global land cover mapping from MODIS: Algorithms and early results," *Remote Sens. Environ.*, vol. 83, no. 1/2, pp. 287–302, 2002.

[42] Oak Ridge National Laboratory Distributed Active Archive Center (ORNL DAA). (2006, Jun. 12). MODIS Subsetted Land Products, Collection 4. [Online]. Available: http://www.daac.ornl.gov/MODIS/modis.html

[43] E. J. Kim and A. W. England, "A yearlong comparison of plot-scale and satellite footprint-scale 19 and 37 GHz brightness of the Alaskan North Slope," *J. Geophys. Res.*, vol. 108, no. D13, pp. 4388–4404, 2003.

[44] E. B. Rastetter, A. W. King, B. J. Cosby, G. M. Hornberger, R. V. O'Neill, and J. E. Hobbie, "Aggregating fine-scale ecological knowledge to model coarser-scale attributes of ecosystems," *Ecol. Appl.*, vol. 2, no. 1, pp. 55–70, Feb. 1992.

[45] F. T. Ulaby, R. K. Moore, and A. K. Fung, *Microwave Remote Sensing: Active and Passive*, vol. 2. Dedham, MA: Artech House, 1986.

[46] N. C. Grody and A. N. Bassist, "Interpretation of SSM/I measurements over greenland," *IEEE Trans. Geosci. Remote Sens.*, vol. 35, no. 2, pp. 360–366, Mar. 1997.

[47] J. S. Kimball, K. C. McDonald, S. Frolking, and S. W. Running, "Radar remotes sensing of the spring thaw transition across a boreal landscape," *Remote Sens. Environ.*, vol. 89, no. 2, pp. 163–175, Jan. 2004.

[48] J. S. Kimball, K. C. McDonald, S. W. Running, and S. Frolking, "Satellite radar remote sensing of seasonal growing seasons for boreal and sub-alpine evergreen forests," *Remote Sens. Environ.*, vol. 90, no. 2, pp. 243–258, Mar. 2004.

[49] J. S. Kimball, K. C. McDonald, A. R. Keyser, S. Frolking, and S. W. Running, "Application of the NASA scatterometer (NSCAT) for classifying the daily frozen and non-frozen landscape of Alaska," *Remote Sens. Environ.*, vol. 75, no. 1, pp. 113–126, Jan. 2001.

[50] Z. Wan, "MODIS land surface temperature algorithm theoretical basis document," *ATBD 3.3*, 1999, Santa Barbara, CA: Univ. California. [Online]. Available: http://modis.gsfc.nasa.gov/data/atbd/land_atbd.php

[51] E. J. Kim and A. W. England, "Diurnal and seasonal cold land signatures in SSM/I-scale microwave radiometery of the North Slope of Alaska," in *Proc. IGARSS*, Jul. 2001, vol. 5, pp. 2127–2129.

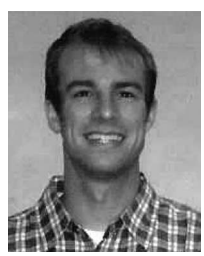

Lucas A. Jones (S'06) received the B.Sc. (Hons.) degree in forestry, with emphasis on terrestrial ecology and remote sensing, from the University of Montana, Missoula, in 2005. He is currently working toward the M.Sc. degree in forestry at the same university.

He is currently a Graduate Research Assistant in the Flathead Lake Biological Station and the Numerical Terradynamic Simulation Group, University of Montana. He was previously with the Fire Sciences Laboratory, Rocky Mountain Research Station, U.S. Department of Agriculture Forest Service, Missoula, MT, and the Tongass National Forest, Ketchikan, AK. His research interests include passive microwave, radar, and optical remote sensing and biophysical modeling for studying carbon and water cycles at multiple temporal and spatial scales, particularly at high latitudes.

Mr. Jones is a member of the American Geophysical Union.

John S. Kimball received the Ph.D. degree in bioresource engineering and geosciences from Oregon State University, Corvallis, in 1995.

He is an Associate Professor of biological sciences at the University of Montana, Missoula. He is a member of the National Aeronautics and Space Administration Earth Observing System MODIS and AMSR-E science teams and is working toward improved measurement and monitoring of global carbon and water cycles through synergistic use of biophysical process models and satellite remote sensing. His research interests include the development and integration of biophysical theory and emerging technologies, including satellite remote sensing and computer simulation and visualization models, for better understanding of terrestrial and aquatic ecosystem structure and function from single plot to global scales.

Kyle C. McDonald (S'89–M'91–SM'98) received the B.S. degree in electrical engineering (cooperative plan with highest honors) from the Georgia Institute of Technology, Atlanta, in 1983, the M.S. degree in numerical science from Johns Hopkins University, Baltimore, MD, in 1985, and the M.S. and Ph.D. degrees in electrical engineering from the University of Michigan, Ann Arbor, in 1986 and 1991, respectively.

He has been a Research Scientist in the Water and Carbon Cycles Group, Earth Science Division, Jet Propulsion Laboratory, California Institute of Technology, Pasadena, since July 2001. He specializes in electromagnetic scattering and propagation, with emphasis on microwave remote sensing of terrestrial ecosystems. He has been a Principal and Co-Investigator on numerous National Aeronautics and Space Administration (NASA) Earth Science investigations. He is a member of the NASA's North American Carbon Program science team, the National Science Foundation's Pan-Arctic Community-Wide Hydrological Analysis and Monitoring Program Science Steering Committee, and the Advanced Land Observation Satellite Phased Array L-band Synthetic Aperture Radar Kyoto and Carbon Initiative science panel. He has been a member of the NASA Boreal Ecosystem–Atmosphere Study (BOREAS) and BOREAS Follow-on science teams, the NASA Scatterometer/Asian Dust and Ocean Ecosystem instrument team, the NASA Ocean Vector Winds Science Team, and the NASA Cold Land Processes Steering Committee. His research interests have primarily involved the application of microwave remote sensing techniques for monitoring seasonal dynamics in boreal ecosystems, as related to ecological and hydrological processes and the global carbon and water cycles. His recent activities have included development of radar instrumentation for measuring sea ice thickness from airborne platforms.

Steven Tsz K. Chan (M'02–SM'03) received the B.Sc. degree in electrical engineering from Portland State University, Portland, OR, in 1993 and the M.Sc. and Ph.D. degrees in electrical engineering from the University of Washington, Seattle, in 1995 and 1998, respectively.

Since 1999, he has been conducting remote sensing research at the National Aeronautics and Space Administration Jet Propulsion Laboratory, California Institute of Technology, Pasadena, where he is currently a Scientist in the Water and Carbon Cycles Group, Earth Science Division. His current research focuses on passive and active microwave remote sensing of soil moisture, long-term variability of global hydrological cycles, and synergy of microwave observations from multiple spaceborne instruments.

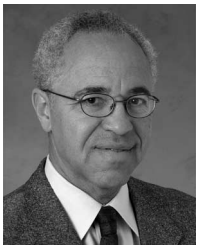

Eni G. Njoku (M'75–SM'83–F'95) received the B.A. degree in natural and electrical sciences from Cambridge University, Cambridge, U.K., in 1972 and the M.S. and Ph.D. degrees in electrical engineering from the Massachusetts Institute of Technology (MIT), Cambridge, in 1974 and 1976, respectively.

From 1976 to 1977, he was a National Research Council Postdoctoral Research Associate. In 1977, he joined the Jet Propulsion Laboratory (JPL), California Institute of Technology, Pasadena, where he is currently a Senior Research Scientist and Supervisor of the Water and Carbon Cycles Group. He is a member of the EOS/Aqua Advanced Microwave Scanning Radiometer science team and, until 2006, was the JPL Project Scientist for the Hydros mission. From 1986 to 1990, he served as a Discipline Scientist for ocean and Earth science data systems at NASA Headquarters, Washington, DC, and, from 1993 to 1994, was the Manager of the Geology and Planetology Section, JPL. During the 2001/2002 academic year, he was on leave as a Visiting Professor in the Department of Civil and Environmental Engineering, MIT. His primary interests are in applications of microwave remote sensing for land surface hydrology and climate. His research involves microwave modeling of the land and ocean surface, retrieval algorithm development, satellite and airborne sensor data analysis for hydrologic applications, and development of new spaceborne observing concepts.

Dr. Njoku is a member of the American Meteorological Society, the American Geophysical Union, the American Association for the Advancement of Science, Commission F of the International Union of Radio Science, and Sigma Xi. He has served as an Associate Editor of the IEEE TRANSACTIONS ON GEOSCIENCE AND REMOTE SENSING (1985–1988), the Technical Program Chairman for IGARSS'94, and a member of the GRSS Administrative Committee (1997–2000). He was a recipient of the NASA Group Achievement Awards in 1980, 1982, and 1985 and of the NASA Exceptional Service Medal in 1985.

Walter C. Oechel received the B.A. degree from San Diego State University, San Diego, CA, in 1966 and the Ph.D. degree from the University of California, Riverside, in 1970.

He is the Director of the Global Change Research Group, San Diego State University.